nature communications

Article

https://doi.org/10.1038/s41467-024-53339-6

Vertically oriented low-dimensional perovskites for high-efficiency wide band gap perovskite solar cells

Received: 30 August 2024

Accepted: 8 October 2024

Published online: 21 October 2024

Check for updates

Andrea Zanetta[1,9], Valentina Larini[1,9], Vikram[2], Francesco Toniolo[1], Badri Vishal[3], Karim A. Elmestekawy[4], Jiaxing Du[4], Alice Scardina[1], Fabiola Faini[1], Giovanni Pica[1], Valentina Pirota[1], Matteo Pitaro[5], Sergio Marras[6], Changzeng Ding[7], Bumin K. Yildirim[3], Maxime Babics[3], Esma Ugur[3], Erkan Aydin[3,8], Chang-Qi Ma[7], Filippo Doria[1], Maria Antonietta Loi[5], Michele De Bastiani[1], Laura M. Herz[4], Giuseppe Portale[5], Stefaan De Wolf[3], M. Saiful Islam[2] & Giulia Grancini[1]

Controlling crystal growth alignment in low-dimensional perovskites (LDPs) for solar cells has been a persistent challenge, especially for low-n LDPs ($n < 3$, n is the number of octahedral sheets) with wide band gaps (>1.7 eV) impeding charge flow. Here we overcome such transport limits by inducing vertical crystal growth through the addition of chlorine to the precursor solution. In contrast to 3D halide perovskites ($APbX_3$), we find that Cl substitutes I in the equatorial position of the unit cell, inducing a vertical strain in the perovskite octahedra, and is critical for initiating vertical growth. Atomistic modelling demonstrates the thermodynamic stability and miscibility of Cl/I structures indicating the preferential arrangement for Cl-incorporation at I-sites. Vertical alignment persists at the solar cell level, giving rise to a record 9.4% power conversion efficiency with a 1.4 V open circuit voltage, the highest reported for a 2 eV wide band gap device. This study demonstrates an atomic-level understanding of crystal tunability in low-n LDPs and unlocks new device possibilities for smart solar facades and indoor energy generation.

Low dimensional perovskites (LDPs), which have been known since the 1990s for transistor applications, represent an interesting family of materials for exploring light-matter interactions and quantum-confined physics and related applications. These materials consist of self-assembled bulky crystals composed of alternating inorganic layers spaced by large organic cations (R), arranged into a $R_2A_{n-1}B_nX_{3n+1}$ structure, where n is the number of inorganic layers stacked together defining the so-called LDP dimensionality[1]. Typically, for A = organic cation, B = lead and X = iodine, if $n < 3$, they are referred to as low-n LDPs, which possess unique optical features such as tuneable band gaps from 2.6 eV to 1.7 eV going from $n = 1$ to $n = 3$, and remarkably stable structures and phase purity[2]. Conversely, high-n LDPs have an

[1]Università Degli Studi Di Pavia - Pavia (Italy), Department of Chemistry & INSTM, Via T. Taramelli 14, Pavia, Italy. [2]Department of Materials, University of Oxford, Oxford, UK. [3]King Abdullah University of Science and Technology (KAUST), KAUST Solar Center (KSC), Physical Sciences and Engineering Division (PSE), Thuwal, Kingdom of Saudi Arabia. [4]Department of Physics, University of Oxford, Clarendon Laboratory, Oxford, UK. [5]Zernike Institute for Advanced Materials, University of Groningen, University of Groningen Nijenborgh 3 (Feringa Building), AG Groningen, The Netherlands. [6]Center for Convergent Technologies, Istituto Italiano di Tecnologia, Via Morego 30, Genova, Italy. [7]i-Lab & Printable Electronics Research Center, Suzhou Institute of Nano-Tec and Nano-Bionics, Chinese Academy of Sciences (CAS), 398 Ruoshui Road, SEID, SIP, Suzhou, China. [8]Now at Department of Chemistry, Ludwig-Maximilians-University, Butenandtstraße 5–13, Munich, Germany. [9]These authors contributed equally: Andrea Zanetta, Valentina Larini. e-mail: giulia.grancini@unipv.it

absorption edge down to 1.5 eV and are often constituted by a mixture of phases where $APbX_3$ co-exists[2]. With their narrower band gap, high-n LDPs have been successfully integrated into efficient perovskite solar cells (PSCs)[3]. Indeed, from a structural perspective, high-n LDPs partially lose their layered structure and are able to efficiently transport the photoinduced charges, assisted by the co-presence of $APbX_3$ phases (as revealed by the edge of external quantum efficiency spectra close to 1.5 eV)[4]. Moreover, induced vertical growth of high-n LDP crystal structures has been demonstrated, further boosting devices' power conversion efficiency (PCE)[5–13]. However, this does not hold true for low-n LDPs where the inorganic frame usually grows parallel to the substrate[14] or self-organizes in a random orientation[15]. Consequently, vertical charge transport and extraction are hindered, strongly limiting the PCE (typically <2%) when integrated into a typical planar device stack[16,17]. This imposes a severe limit to low-n LDP applications, despite their wide band gap being ideal for semi-transparent devices and building integrated photovoltaics (PVs)[18,19]. By solving these limitations, low-n LDPs would have advantages over the conventional high band gap solutions based on mixed halide (Br/I) $APbX_3$ perovskites such as methylammonium lead halides ($MAPbX_3$)[20], which still suffer from structural instability and light-induced halide segregation, causing open-circuit voltage (V_{OC}) losses and performance reduction[21–24]. Therefore, to go beyond the state-of-the-art, it is imperative to develop a method to control the tilting and alignment of the inorganic framework of the low-n LDPs with respect to the substrate[15], which would be a major advance for wide band gap PSCs.

In this work, we use thiophenemethylammonium iodide (TMAI) as the R cation to form a vertically oriented $n = 2$ LDP with a band gap of ~2 eV, which we successfully integrate into a planar device stack. We then demonstrate a highly efficient 2 eV wide band gap vertically oriented LDP solar cell, overcoming the current transport limits. This has been obtained by elucidating the critical role of Cl in dictating vertical crystallization. In contrast to the current knowledge on 3D $MAPbX_3$ perovskites, we found that a small degree of Cl substitutes for I in the PbI_6 octahedra leading to an expansion of the unit cell in one direction, which is critical in inducing vertical alignment as corroborated by joint experimental and ab initio modelling analysis. Integrated into a solar cell, the vertical orientation is preserved through the whole device thickness, ensuring efficient charge transport and resulting in a champion 9.4% PCE, which is, to the best of our knowledge, the highest PCE reported for a PSC based on a low-n 2 eV band gap LDP. The concept is also validated on a semi-transparent solar cell, demonstrating the potential exploitation of low-n LDPs in coloured and transparent PVs.

Results

Thin film fabrication and GIWAXS analysis

Figure 1 schematically represents the preparation procedures for low-n LDPs with the chemical formula $TMA_2MAPb_2I_7$ ($n = 2$). The standard method (Fig. 1a) involves the dissolution of the stoichiometric ratio of precursor powders in dimethylformamide (DMF) and the subsequent spin coating and annealing steps. The structure and texture of the resulting thin films were investigated by grazing incident wide-angle X-ray scattering (GIWAXS), whose results are reported in Fig. 1b. The unit cell can be identified as being very close to orthorhombic with axes $8.8 \times 41.5 \times 8.7$ Å and with $\beta = 87°$, in close agreement with previous reports[25]. Since the (0k0) reflections are predominantly oriented along the q_z direction, the crystallites orient with their (0k0) planes parallel to the substrate, meaning the inorganic slabs are oriented horizontally (Fig. 1c). This is the most common orientation reported for low-n LDPs (named horizontal hereafter)[14].

In Fig. 1d the developed method is outlined, in which we employ a partial substitution of methylammonium iodide (MAI) with methylammonium chloride (MACl) at different concentrations (see Supplementary Fig. 1); this was further optimized at a 30:70 ratio (MAI:MACl) and by adding an annealing step of the mixed precursor solution at 60 °C for 2 h, before its deposition. The MAI:MACl ratio corresponds to an optimal 10% total amount of Cl substituting I in the perovskite formulation. When 10% Cl is added, the GIWAXS pattern (Fig. 1e) drastically changes revealing that the (0k0) reflections are now oriented along the qy direction. This indicates a switch of crystallite orientation such that the inorganic slabs are now vertically oriented with respect to the substrate. Notably, the signals appear more arch-like because of a certain degree of structural disorder and misalignment with respect to the pure $TMA_2MAPb_2I_7$ phase. As reported in Fig. 1f, two main orientations of the unit cell are detected for the films produced with our formulation: crystallites are now oriented either with the (001) or with the (101) planes parallel to the substrates. In both orientations, the inorganic slabs are vertically aligned (sample named vertical hereafter), as depicted in Fig. 1f.

To ultimately confirm the different crystal structure orientation of horizontal and vertical samples, we perform a texture analysis through advanced X-Ray Diffraction (XRD) Pole Figure (PF) investigation, whose results are reported in Fig. 1g. By comparing the experimental PFs with the Wulff Stereographic Projections (WSPs) for a single crystal perfectly aligned along the [101] (in red) and [010] (in yellow) crystallographic directions, we investigate the orientation of three different lattice planes: (202) (Fig. 1g), (151) and (080) (Supplementary Fig. 2) that correspond to reflections at 28.73°, 17.83°, and 17.11°, respectively. In the case of the horizontal LDP, the PF (202) presents higher intensity in the outer ring coinciding with the diffraction of the [101] family of planes. These are responsible for the central peak of PF (080), confirming that in the horizontal sample, the vertical orientation of the inorganic layer is not present, in agreement with the GIWAXS results. Conversely, the strong peak at the centre of PF (202) for the vertical sample confirms such preferential growth along the [101] direction in which crystals tend to grow with a fibre-textured disposition perpendicularly to the substrate, which is also confirmed by the ring observed in the PF (151) corresponding to the tilted plane reflections. Overall, the structural analysis shows the effectiveness of our strategy in directing the vertical growth on the low-n LDP thin films.

Optical and photoconductivity analysis of LDP thin films

The optical properties of the low-n LDP thin films do not depend on the material crystallization. Indeed, the different samples absorption spectra are identical, displaying a sharp onset at 2.1 eV (as calculated from the Tauc plot in Supplementary Fig. 3) and a clear excitonic peak at 567 nm (Fig. 2a), typical of a $n = 2$ LDP. We note that the horizontal sample shows a minor shoulder at longer wavelengths, indicative of a small fraction of $n = 3$ phase, which also appears in the steady state photoluminescence (PL) spectra together with the peak related to the $n = 2$ phase (see Supplementary Fig. 4). To gain a demonstration of the material stability, we monitor the PL peak position exposing the films under continuous 1 Sun AM1.5G illumination and thermal stress at 60 °C (Supplementary Fig. 5). In both cases no variations are observed, indicative of a high robustness and phase integrity against UV light and thermal stressors.

To investigate the effect of vertical alignment on the charge-carrier transport properties, we start by analysing the electronic structure of $TMA_2MAPb_2I_7$ (shown in Fig. 2b), obtained using density functional theory (DFT) calculations. The primitive cell of $TMA_2MAPb_2I_7$, along with the Brillouin zone showing the high symmetry directions, are shown in Supplementary Fig. 6. $TMA_2MAPb_2I_7$ has a direct band gap at the Γ-point. The flat bands along the high symmetry direction Γ-Y indicate heavy carriers perpendicular to the PbI_6 plane, while the more dispersive bands along Γ- Δ_0, and Γ-Z directions suggest lighter carrier transport within the plane. This is corroborated by the effective mass values (inset Fig. 2b) along the three axes of the conventional unit-cell, which are higher along the vertical b-axis and moderate along the horizontal a- and c-axes for both

https://doi.org/10.1038/s41467-024-53339-6

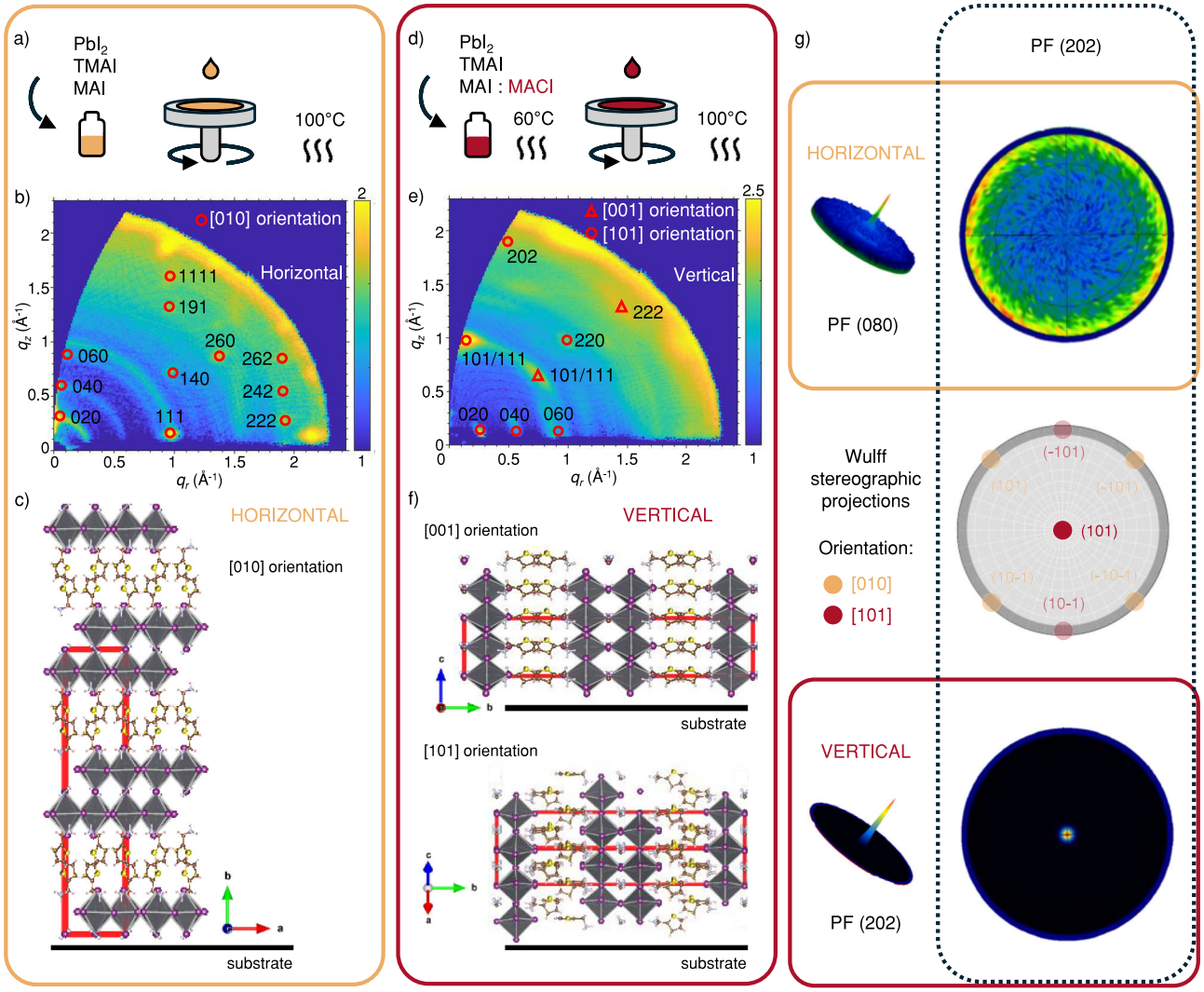

Fig. 1 | Preferential horizontal and vertical orientation of LDP thin films. **a** Schematic representation of the fabrication method for $TMA_2MAPb_2I_7$ LDP thin films. **b** GIWAXS results and **c** crystal structure orientation of horizontal LDP thin films. Crystal planes are oriented along the [010] direction. **d** Schematic representation of the fabrication method for $TMA_2MAPb_2I_7$ LDP thin films fabricated by substituting 70% of MAI with MACl. **e** GIWAXS results and **f** crystal structure orientation of vertical LDP thin films. Crystal planes are oriented along two different directions, namely [101] and [001], both of which are perpendicular to the substrate. **g** PF images for horizontal (at the top) and vertical (at the bottom) LDPs for (202) lattice plane and Wulff stereographic projections for the [010] and [101] orientations.

electron and hole carriers. The calculated effective masses are in good agreement with previous reported values for LDPs[26]. These results demonstrate that carrier transport can be significantly enhanced by growing these LDPs with vertical alignment.

In order to further assess how the different orientations of the LDP planes impact charge-carrier transport at the nanoscale level, we employ optical-pump THz-probe photoconductivity spectroscopy. A sub-ps laser pulse at 3.1 eV excites the LDP films, and the resulting photoconductivity is recorded for a range of fluences, as shown in Fig. 2c and d for samples with horizontal and vertical layer orientation with respect to the substrate, respectively. We may further extract the effective electron-hole sum mobility from the conductivity recorded immediately after photoexcitation, under knowledge of the absorbed photon density (see methods section). We note that since the electric field of the THz probe pulse oscillates at right angle with respect to its propagation through the substrate, such mobility values reflect charge-carrier motion within the thin-film plane, parallel to the substrate. Figure 2e and f show that these films indeed exhibit the expected behaviour for highly oriented LDP films. A high in-plane mobility of 4.9 $cm^2V^{-1}s^{-1}$ is observed when the THz electric field oscillates fully along the LDP planes, for the horizontal samples. For the vertical sample, on the other hand, the E-field vector lies on average half along the LDP planes, and half in the direction vertical to the planes. The observed mobility of 2.2 $cm^2 V^{-1} s^{-1}$ is indeed lowered by nearly a factor of 2, as would be expected given the insignificant mobility of charges across spacer layers (in line with the effective mass values in Fig. 2b), confirming the highly oriented nature of the LDP films[27,28].

Insights into chlorine effects on vertical crystallisation

We now focus our attention on the fundamental question: why does the addition of Cl have such a strong impact on guiding the vertical crystallization? For standard $MAPbX_3$ perovskites, it is well known that MACl-assisted perovskite crystallization favours the α-phase (with respect to non-perovskite phases, as in the case of formamidinium-based perovskites)[29,30], and that Cl sublimates during the process[31]. In order to verify the presence of Cl and map its content, we performed time-of-flight secondary ion mass spectroscopy (ToF-SIMS), as shown in Fig. 3a and b for the horizontal and vertical samples, respectively. For the horizontal sample Cl is absent, comparable in intensity to the

https://doi.org/10.1038/s41467-024-53339-6

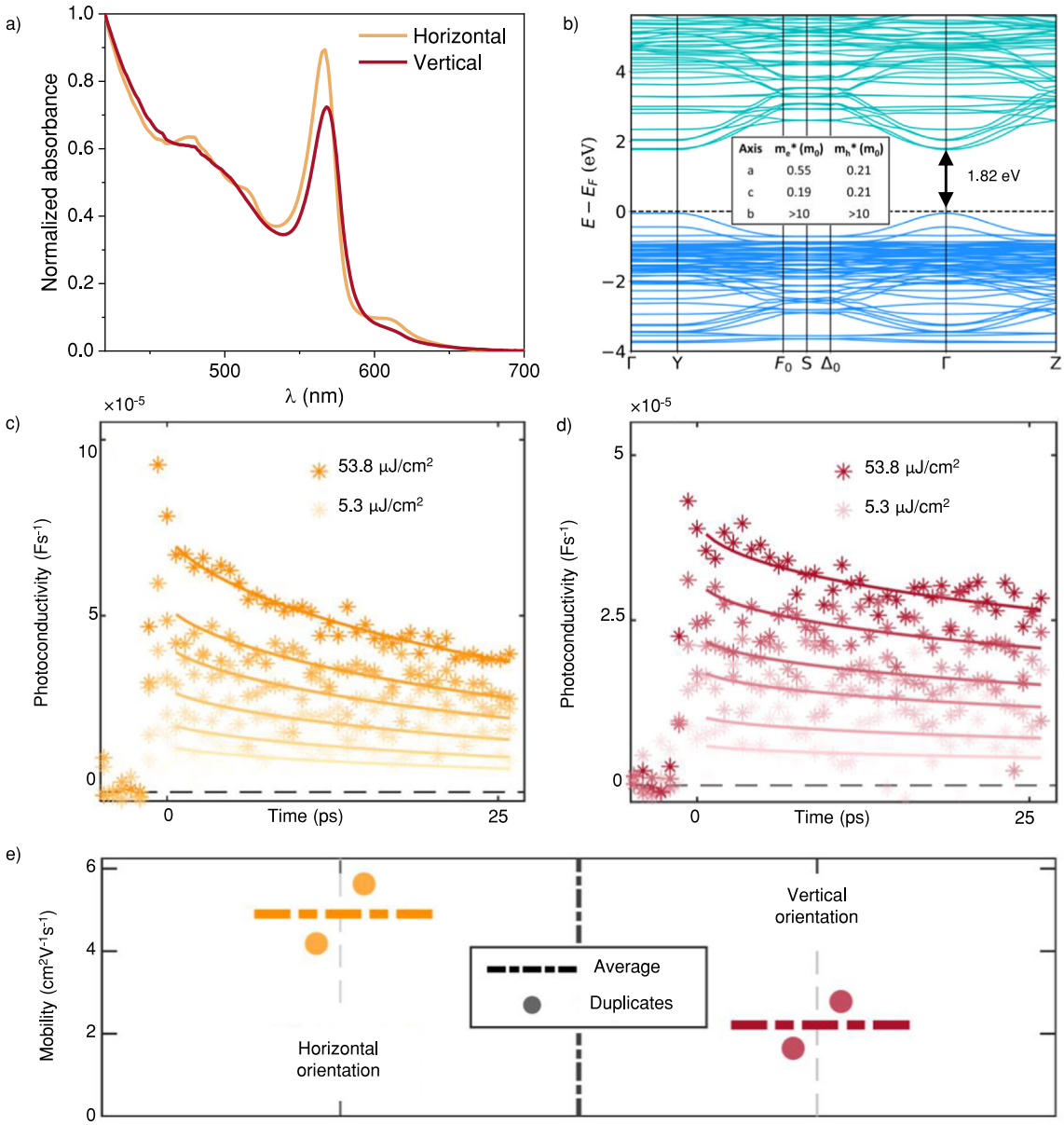

Fig. 2 | Optical and photoconductivity measurements. a Normalized UV-Vis absorbance spectra of horizontal (in yellow) and vertical (in red) LDP thin films. **b** Electronic band structure of $TMA_2MAPb_2I_7$ from DFT simulations with the inset showing the electron and hole effective masses along the three conventional unit cell axes. Photo-induced sheet THz conductivity dynamics of the **c** horizontal (in yellow) and **d** vertical (in red) LDP thin films. The excitation fluence (excitation intensity per laser pulse) was varied from 5.3 μJ cm^{-2} up to 53.8 μJ cm^{-2} in a similar manner for both types of LDP thin films. **e** Effective electron-hole sum mobility estimates extracted from the conductivity values immediately post photoexcitation. Such analysis corroborates the vertical alignment of the inorganic chain as detected by X-rays, resulting in a corresponding boost in the charge-carrier mobility.

background signal. In contrast, in the vertical sample there is a gradient distribution of Cl which maximizes at the indium tin oxide (ITO)/perovskite interface. In addition, for both horizontal and vertical LDPs, the CN, I and S signals are uniformly distributed across the whole film thickness.

To further deepen our understanding on Cl inclusion in the film, we conducted a combined experimental and computational modelling analysis, whose results are reported in Fig. 3c–f. First, by closely comparing the GIWAXS profiles of the two samples, a shift in the (0k0) peaks is observed (Fig. 3c). The pattern of the vertical sample can be indexed by a slightly larger orthorhombic unit cell, especially along the axis perpendicular to the octahedra, with axes 8.5 × 42.5 × 9.0 Å (with respect to 8.8 × 41.5 × 8.8 Å for the horizontal sample). The expansion of the long axes can be the result of Cl incorporation inside the crystal unit, leading to structural distortion and lattice expansion. While Cl inclusion in the unit cell is known to be energetically unfavourable in $MAPbX_3$ perovskites, the situation appears to be different for low-n LDPs, due to their layered, quantum-confined structure. Cl partially substitutes I in the equatorial position, creating a strain in the octahedra and thus elongating the unit cell along the vertical axes. Such vertical compression induces a switch in crystal orientation, responsible for the vertical alignment. A similar structural effect, where Cl incorporates in the equatorial position substituting I, has been recently demonstrated in LDP quantum confined nanocrystals, strongly corroborating our results[32].

To verify our hypothesis and gain additional atomic-scale insights into Cl incorporation in $TMA_2MAPb_2I_7$, we have used DFT-based methods to investigate the thermodynamic stability and miscibility of Cl-mixing at I-sites. The positive mixing energies for all the structures between $0 < x < 0.21$ and $0.79 < x < 1$ in $I_{1-x}Cl_x$ (Supplementary Fig. 7)

https://doi.org/10.1038/s41467-024-53339-6

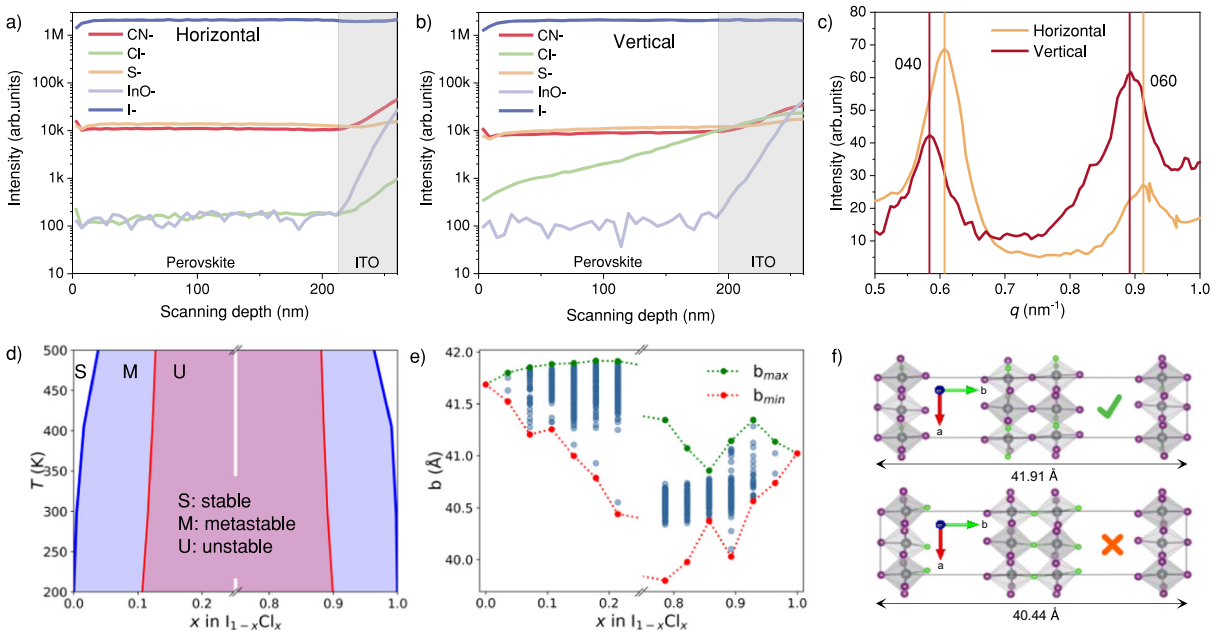

Fig. 3 | Chloride inclusion in the crystal structure. ToF-SIMS analysis of **a** horizontal and **b** vertical thin films deposited onto ITO substrates, showing an increasing Cl distribution from the surface towards the bottom edge of the vertical sample. **c** GIWAXS pattern of horizontal (in yellow) and vertical (in red) LDP thin films in the 0.5–1 nm^{-1} q range. **d** Simulated phase diagram for the thermodynamic analysis of Cl-incorporation at I-sites in $TMA_2MAPb_2I_7$ and, **e** b-lattice parameter for 1121 different DFT optimized structures randomly and uniformly distributed over $0 < x < 0.21$ and $0.79 < x < 1$ for x in $I_{1-x}Cl_x$. For clarity, to show the stability region (white, marked S), we have broken the x-axis at x = 0.21 and 0.79, between which the unstable region (pink, marked U) continues. The metastable region is indicated by the blue shadowing and marked with M. **f** Unit cells of x = 0.21 Cl at I-sites with the maximum (top) and minimum (bottom) b-lattice parameters. The spacer cations are omitted for clarity.

indicate a low tendency for Cl/I mixing, although the structures near the end points (x = 0, 1) can be accessible at finite temperatures. The thermodynamic stability phase diagram is shown in Fig. 3d. Three important features emerge. First, a stability region exists close to the I-rich (x = 0) and Cl-rich (x = 1) regions over 300 K, which grows with an increase in temperature. This indicates that Cl can be incorporated into I-sites in small amounts (~2% at 373 K). Second, small metastable regions exist within 10% of the I-rich and Cl-rich regions ($x < 0.1$ and $x > 0.9$) for the entire temperature range. Being thermodynamically metastable, these states may be accessed and made kinetically stable via alternate synthesis methods. Third, the I/Cl-mixing states are unstable in the wide range of $0.1 < x < 0.9$. Overall, these results show that it is possible to incorporate Cl at I-sites, but only in small amounts.

Next, we examined the b-lattice parameter variation of all the structures between $0 < x < 0.21$ and $0.79 < x < 1$ in $I_{1-x}Cl_x$ to investigate the structural distortion upon Cl addition (Fig. 3e; further analysis of the structural and energetic variation with Cl content is shown in Supplementary Figs. 8,9). Interestingly, compared to the structures with the minimum b-lattice parameter at each concentration, the structures with the maximum b-parameter (i) are energetically favoured, (ii) have a preferred equatorial distribution of Cl at I-sites (Fig. 3f), and (iii) have larger spacer cation distances. Examining the energetically most stable structures at each concentration, Cl ions are found to be predominantly distributed at the equatorial I-sites. The structures with the highest b-lattice parameter have lower unit cell volumes due to compression along the a- and c-lattice parameters. Analysis of the N-C-C and C-S-C bond angles of the spacer cations from $0 < x < 0.21$ indicate that there is no major stretching of the spacer cation ring, whereas the terminal N-C-C bonds are affected by the presence of highly electronegative Cl^- ions in close vicinity. In summary, the equatorial distribution of Cl is energetically preferred, which causes compressive strain on the unit cell along the a- and c-lattice parameters. This creates steric hindrance among the spacer cations, leading to an elongation of the b-parameter, which is in line with our GIWAXS results.

Finally, by testing the effects on crystal orientation of other Cl^- sources such as thiophenemethylammonium chloride (TMACl) and lead chloride ($PbCl_2$) (Supplementary Fig. 10), we could ultimately confirm the role of the anion on triggering verticalization.

Device characteristics and performance

We integrate our vertical low-n thin film into a p-i-n PSC, with the key aim of demonstrating the proof-of-concept of an efficient wide band gap LDP solar cell and ultimately breaking current limits. First, to verify that the vertical orientation is preserved when the perovskite is sandwiched in a device stack composed of a self-assembled monolayer (SAM)-modified oxide and a fullerene derivative electron acceptor, we performed high-angle annular dark-field scanning transmission electron microscopy (HAADF-STEM), whose results are reported in Fig. 4a. From the cross-section images, all the different layers comprising the device stack are visible (elemental mapping is shown in Supplementary Fig. 11). The grains of the vertical LDP layer are arranged in a columnar fashion, perpendicularly to the substrate, with a length of the nano-pillars of the order of 300 nm covering the entire thickness of the active layer. By increasing the resolution through the high-resolution TEM (HR-TEM) technique, we could further investigate the alignment of the inorganic backbone and assess the purity of the low-n LDP phase. As shown by the central panel of Fig. 4a, the vertical features can be ascribed to the layered structure of the LDP, in which the bright areas represent the organic sheets (with a spacing of about 13.06 Å) and the dark lines corresponds to the stack of two PbI_6^- octahedra layers. Furthermore, the right image of Fig. 4a shows HR-TEM and corresponding Fast Fourier Transform (FFT) along zone axis <001>, which confirms that the lattice parameters of the material correspond to those of a pure $n = 2$ LDP phase (a = b = 7.36 Å) (no higher n phase are detected)[33].

https://doi.org/10.1038/s41467-024-53339-6

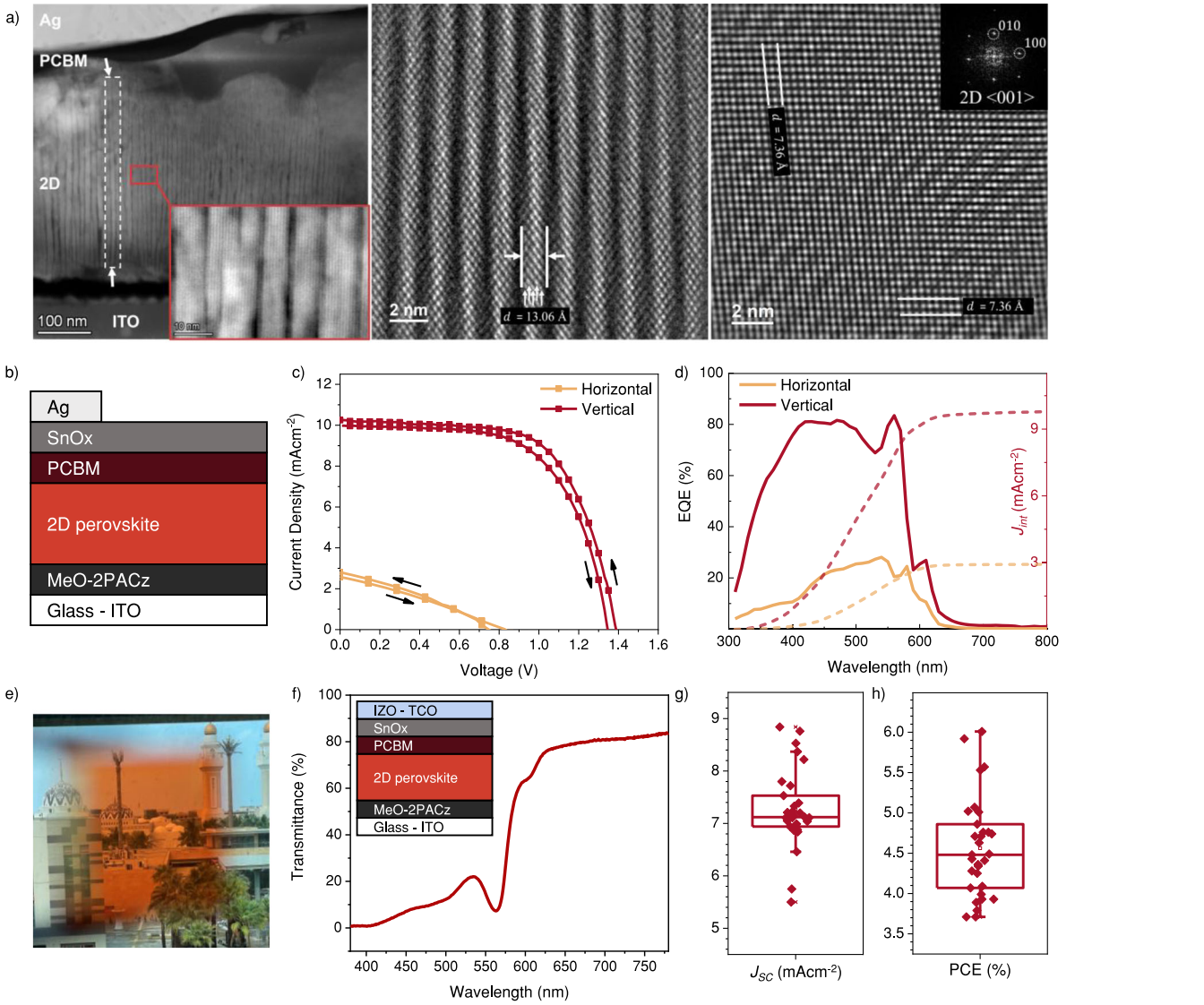

Fig. 4 | Photovoltaic performance of PSCs and semi-transparent devices. a TEM analysis of PSCs fabricated with vertical LDP as active layer: large area cross-sectional HAADF-STEM and HR-HAADF-STEM images of the device (left). HR-TEM of a single inorganic stack of vertical $n = 2$ LDP (centre); white arrows represent 5 atom stacks that compose the inorganic layer of the material. HR-TEM and corresponding FFT (right) of LDP along zone axis <001>. **b** Schematic representation of a p-i-n PSC adopting horizontal and vertical LDPs as active layer, (2-(3,6-Dimethoxy-9H-carbazol-9-yl)ethyl)phosphonic acid (MeO-2PACz) as hole transport layer (HTL), (6,6)-Phenyl C61 butyric acid methyl ester (PCBM) and tin oxide (SnO_X) as electron transport layer (ETL) and Ag as metal contact. **c** *J-V* curves (reverse and forward scan) of champion PSCs fabricated with vertical and horizontal LDPs as active layers. The inset shows the architecture of the device under investigation. **d** EQE and J_{int} of horizontal (in yellow) and vertical (in red) LDPs-based devices. **e** Picture of a semi-transparent PSC fabricated employing the vertical LDP as active layer, MeO-2PACz as HTL, PCBM and SnO_X as ETL and IZO as top contact. **f** Light transmittance of the full device from which AVT has been calculated. The inset shows the architecture of the device under investigation. **g** J_{SC} and **h**) PCE box charts of semi-transparent PSCs fabricated employing the vertical LDP as active layer. Sample size is 25. Whiskers limit the 1.5 interquartile range, the box identifies the 25th and 75th percentile and the horizontal line and the empty square represent the median and mean values, respectively.

A schematic of the device is presented in Fig. 4b. Figure 4c shows the characteristic current density (J)-voltage (V) curve for champion PSCs fabricated with horizontal and vertical LDPs in both forward and reverse scan. The horizontal PSC displays a PCE of 0.8%, strongly limited by the short-circuit current density (J_{SC}), as commonly observed in the literature, due to the charge transport barrier[34]. In contrast, the vertical device shows a PCE of 9.4%, strongly outperforming its horizontal counterpart, with a J_{SC} of 10.6 $mAcm^{-2}$, a fill factor (FF) of 63.2%, and a V_{OC} of 1.40 V. To the best of our knowledge, this proof-of-concept device shows the highest PV parameters reported thus far for a 2 eV band gap LDP (i.e. composed of a low-n LDP, see Supplementary Table 1 and Supplementary Fig. 12 for comparison with literature results). A statistical analysis by box charts for the PV parameters of horizontal and vertical PSCs is reported in Supplementary Fig. 13.

Figure 4d shows the external quantum efficiency (EQE) and integrated current density (J_{int}) curves for horizontal and vertical devices. At lower wavelengths, the EQE signal is significantly different for the two samples. The vertical device achieves values higher than 80%, whereas the horizontal barely overcomes 25% over the visible range. As the absorption spectra of the two samples are very similar, the reason behind the higher photocurrent is ascribed to the different crystal orientation which provides a route for efficient charge transport. Moreover, the EQE spectrum, and specifically its sharp onset at 2 eV,

provides strong evidence of the phase purity of our low-n LDP active layer, setting the demonstration for a wide band gap low-n LDP to generate such a high photocurrent. Furthermore, we tested the stability of both vertical and horizontal devices by maximum power point tracking (MPPT) under 1 Sun AM1.5 G illumination. As shown in Supplementary Fig. 14, stability measurements reported in the literature show that devices fabricated with 2 eV band gap, 3D mixed halide perovskites reach the 80% of their initial PCE in a few minutes (T_{80} = 400 s and 1 h for refs. 35 and[36], respectively). In contrast, T_{80} for our vertical device is 150 h, demonstrating that the vertical orientation of the crystal structure is beneficial to stability.

Finally, to broaden the scope of our concept, we tested our vertical low-n LDP active layer in semi-transparent devices (Fig. 4e), by substituting the opaque Ag electrode with an indium zinc oxide (IZO) transparent electrode (Fig. 4f, inset). The light transmission analysis, represented in Fig. 4f, shows the high transmittance of the device that reaches values higher than 80% in the region > 620 nm, resulting in a calculated average visible transmittance (AVT) for the device of 31%, which meets the requirements for window-integrated PV applications. As presented in Fig. 4g and h and in Supplementary Fig. 15, devices exhibit average values of 1.26 V for V_{OC}, 7.3 mAcm^{-2} for J_{SC}, 50% for FF and 4.6% for PCE, resulting in a light utilization factor (LUE) of 1.86%, which is similar to 3D perovskites-based semi-transparent devices previously reported[37,38].

Discussion

In conclusion, our work demonstrates that low-n LDPs can effectively represent a breakthrough strategy for wide-band gap solar cell applications. This approach is made possible by achieving a phase pure low-n LDP thin film featuring vertical crystallization of its inorganic backbone, which allows efficient charge transport. The orientational switch, as demonstrated here by a combined experimental and modelling study, is triggered by Cl incorporation in the unit cell structure which substitutes for I in the equatorial position. As a result, the unit cell is compressed featuring a vertical strain which induces the crystal orientation. In contrast to 3D ABX_3 perovskites including $MAPbI_3$, such substitution is thermodynamically favoured in LDPs possibly due to their intimate layered nature, representing a fundamental advance in atomistic understanding. When integrated into a working solar cell the verticalization is preserved, demonstrating a highly efficient low-n LDP solar cell with a 2 eV band gap. This concept represents a viable alternative for visible light harvesting wide band gap applications, ranging from building integrated PVs to indoor light harvesting and multi-junction PV devices.

Methods

Materials

Solvents were purchased from Sigma-Aldrich (highest purity and anhydrous); lead iodide (PbI_2, 99.99% purity) and (2-(3,6-Dimethoxy-9H-carbazol-9-yl)ethyl)phosphonic acid (MeO-2PACz) were purchased from TCI; organic iodide salts (MAI, MACl, TMAI) were purchased from GreatCell Solar. (6,6)-Phenyl C61 butyric acid methyl ester (PCBM, >99.5%) was purchased from Lumtec; Bathocuproine (BCP, sublimed grade, 99.99% purity) was purchased from Sigma Aldrich. Unless otherwise specified, materials and solvents have been used as received. All the solutions/dispersions were prepared into an Ar-filled glovebox and the spin coating steps were carried out into a N_2-filled glovebox (in both case, O_2 concentration <0.1 ppm and H_2O concentration <0.1 ppm).

Low-dimensional perovskite thin film and solar cell fabrication

The precursor solution (0.7 M) for the horizontal $TMA_2MAPb_2I_7$ (n = 2) LDP was prepared by mixing stoichiometric ratio of TMAI, MAI and PbI_2 powders in DMF. In the case of the vertically oriented LDP, 70 mol% of MAI was replaced by MACl, without changing the total stoichiometric amount of MA in the solution. After complete dissolution, the solution was subjected to a thermal annealing step of 2 h at 60 °C. The solution was deposited onto glass substrates via single-step spin coating procedure at 4000 rpm, 2000 rpm s^{-1} acceleration for 40 s. 120 µl of toluene was dropped onto the spinning substrate at 20 s before the end of the programme for anti-solvent procedure. Subsequently, samples were annealed at 100 °C for 30 min.

For PSCs fabrication, prepatterned ITO/glass substrates were sequentially cleaned with acetone and 2-propanol (IPA) by ultrasonication for 15 min in each solvent. ITO/glass substrates were then dried with N_2 and treated with oxygen plasma at 100 mW for 10 min. Then, substrates were moved into a N_2-filled glovebox for subsequent layers deposition. MeO-2PACz self-assembly monolayer was deposited by spin coating (3000 rpm, 30 s, 1500 rpm s^{-1}) a 0.335 mg mL^{-1} solution in ethanol, followed by annealing at 100 °C for 10 min. The LDP layer was fabricated following the same procedure employed to prepare thin films. A PCBM solution (20 mg mL^{-1} in chlorobenzene) was deposited onto the perovskite by dynamic spin coating at 2000 rpm, with an acceleration of 1000 rpm s^{-1} for 30 s, followed by 10 min annealing at 100 °C. Finally, 20 nm of SnO_2 were deposited by atomic layer deposition (ALD, Picosun) and 80 nm of Ag were thermally evaporated, producing pixels with 0.045 cm^2 active area (shadow mask aperture area estimated by optical microscopy).

For semi-transparent devices, 100 nm of IZO was sputtered (Angstrom EvoVac) onto the SnO_2 buffer layer as top contact electrode (pixels active area ~0.1 cm^2).

Grazing incident wide-angle X-ray scattering

GIWAXS experiments have been performed at the MINA instrument at the University of Groningen. The instrument is built around a Cu rotating anode source, delivering a high-power X-ray beam with a photon energy of 8 keV (λ = 0.15413 nm). The samples have been measured in GI geometry, using an incident angle of 1°, which ensures full penetration of the sided LDL films. The films were measured in a primary vacuum to avoid air scattering and sample degradation during the measurements. GIWAXS patterns were collected using a Vantec500 Bruker detector with 0.068 × 0.068 mm x mm pixel dimension placed 10 cm away from the sample. The angular range was calibrated using the diffraction peaks from a standard Al_2O_3 sample and data analysis was conducted using the GIXSGUI Matlab-based programme[39].

Pole figure

Pole Figure (PF) technique is based on the acquisition of XRD data by varying the incidence angle along two different axes to build PF maps. In such way, different orientations of crystalline samples are proved and compared with the Wulff Stereographic Projection (WSP) calculated from single crystal data. Pole Figure (PF) analysis was performed with the detector set in 0D mode, using 0.04 rad soller slits and 0.28° parallel plate collimator (PPC) on the diffracted beam. This configuration allows a maximum sample tilt equal to χ = 85°. Simulated pattern for the $TMA_2MAPb_2I_7$ n = 2 LDP perovskite was obtained with CrystalDiffract 6.9.4 from CrystakMaker Software Ltd. Pole Figure analysis was carried out using X'Pert Texture 1.3 software from PANalytical. The Wulff stereographic projections (WSP) were created using WinWulff 1.6 from JCrystalSoft.

UV-Vis absorption

The absorption spectra of the perovskite thin films were collected using a UV-NIR spectrophotometer from Perkin Elmer (Lambda 1050+).

Photoluminescence measurements

The photoluminescence (PL) spectra of the different samples were collected using a customized optical setup[40] in which the excitation was provided by pulsed/CW laser at 470 nm (PicoQuant), while the

luminescence was analysed with an interferometer (GEMINI by Nireos) and recorded with a single photon detector (IDQuantique) coupled with a Time Tagger (Swabian Instrument).

Computational modelling

First-principles simulations were performed within the framework of density functional theory (DFT) as implemented in the Vienna Ab-initio Simulation Package (VASP)[41–43] using a projector augmented-wave (PAW)[44] basis. The generalized gradient approximation (GGA) exchange-correlation functional of Perdew Burke-Ernzerhof (PBE)[45] was used for all the structures. VASP-recommended PAW pseudopotentials were used for all the atomic species (C:$2s^2 2p^2$, N:$2s^2 2p^3$, H:$1s^1$, S:$3s^2 3p^4$, Pb:$5d^{10} 6s^2 6p^2$, I:$5s^2 5p^5$, and Cl:$3s^2 3p^5$). Grimme's DFT-D3 dispersion correction[46] was considered due to the presence of organic molecules. A plane wave energy cut-off of 500 eV and a Brillouin zone sampling using Γ-centred k-mesh are employed done REMOVE DONE for all the calculations. A k-point grid of 3 × 1 × 3 with a Gaussian smearing of 0.1 was used for structure optimization whereas a k-point grid of 6 × 2 × 6 with Gaussian smearing of 0.01 was used to obtain accurate charge densities to calculate the electronic structure. The cell volume, shape, and atomic positions were fully relaxed using the conjugate gradient algorithm until the force on each atom converged below 0.01 eV $Å^{-1}$. The self-consistent energy convergence of 10^{-6} eV was used for electronic degrees of freedom.

The carrier effective masses were calculated using the Effective Mass Calculator (EMC) code[47]. We used the Site-Occupation Disorder (SOD) code[48] to generate symmetrically inequivalent structures in the orthorhombic space group Aba2 (#41) for $0 < x < 0.21$ and $0.79 < x < 1$ in $I_{1-x}Cl_x$. It is unfeasible to enumerate the thousands of symmetrically inequivalent structures for $0.21 < x < 0.79$ in $I_{1-x}Cl_x$. Therefore we used the icet code[49] to generate randomly occupied structures in this compositional range. The thermodynamic stability phase diagram for Cl mixing at I-sites was calculated using the Generalized Quasi-Chemical Approximation (GQCA)[50], which has been effectively utilized in the thermodynamic analysis of perovskite materials[51–53]. 235 lowest energy-optimized structures distributed uniformly over each possible concentration from $0 < x < 1$ in $I_{1-x}Cl_x$ were used to generate the thermodynamic stability phase diagram. 1121 different structures chosen randomly and distributed uniformly between $0 < x < 0.21$ and $0.79 < x < 1$ in $I_{1-x}Cl_x$ were optimized to analyse the preferred distribution of Cl and their effects on the lattice distortion.

THz photoconductivity and mobility measurements

An amplified laser system (Spectra Physics, MaiTai – Ascend – Spitfire), with a 5 kHz repetition rate, centre wavelength of 800 nm and pulse duration of 35 fs is used to generate the THz radiation using a spintronic emitter. The THz probe is then focused onto the sample, overlaid with a 400 nm excitation pump that is generated using a Beta Barium Borate (BBO) crystal. The THz radiation transmitted through the sample is then detected via free-space electro-optical sampling in a ZnTe (110) crystal of thickness 200 μm[54].

The variations in the THz transmission $\Delta T\ T^{-1}$ through the sample can therefore be measured, and temporally resolved by varying the time delay between the optical pump and the probing THz pulses in order to obtain the temporal evolution of the photo-induced conductivity of the sample[51,52].

Additionally, for low enough laser fluences and charge-carrier densities, the sum mobility of free charge carriers will have a linear dependence on photoconductivity values and can therefore lead to an extraction of the intrinsic effective sum mobility based on the early time conductivity values post photoexcitation[55,56].

We also ascertained that the THz mobility values extracted within the first picoseconds indeed solely reflected the motion of charge carriers within the $n = 2$ LDP phase, by also recording time-resolved photoluminescence spectra, using a time-correlated single photon counting (TCSPC) device following excitation by a 398 nm picosecond pulsed diode laser (PicoHarp, LDH-D-C-405M). These PL measurements showed that over the first nanoseconds of charge-carrier lifetimes for which the THz photoconductivity transients were recorded, the PL solely reflected emission from an $n = 2$ LDP phase.

Time-of-flight secondary ion mass spectroscopy

ToF-SIMS analyses were acquired with ToF-SIMS 5–100, with the pulsed primary ions from a Cs^+ (2 keV) ion gun for sputtering and a Bi^+ ion beam (30 keV) for analysis.

Transmission Electron Microscopy

Transmission electron microscopy (TEM)-based experiments were conducted in both parallel beam mode high-resolution TEM (HRTEM) and converge beam scanning TEM (STEM) mode. The HRTEM experiments were performed in Cs spherical aberration image-corrected Thermo Fisher Titan 60–300 Cubed TEM microscope. In STEM mode, High-Angle Annular Dark-Field STEM HAADF-STEM) imaging combined with Energy Dispersive Spectroscopy (STEM-EDS) was executed for elemental mapping on Cs-aberration-probe-corrected Thermo Fisher Titan 60–300 Cubed TEM microscope operating at 300 kV. TEM data processing was performed using Gatan™ Digital Micrograph and Thermo Scientific™ Velox suites. For the TEM study, cross-sectional electron-transparent lamella was prepared in a focused ion beam (FIB) equipped scanning electron microscope (SEM-FIB Helios G4 DualBeam, FEI) with the help of an EasyLift nanomanipulator and Ga ion source. To protect the region of interest during FIB, two types of protective coatings were deposited: a 0.5 μm layer of Pt coating deposited by the e-beam, followed by a 3 μm layer of Pt coating deposited by the ion beam for final protection. Step-by-step ion beam milling procedure with beam current (2.4, 0.44, 0.26, 0.045, 0.025 nA for 30 to 5 kV) was carried out by cutting and thinning down lamella to 60 nm while decreasing beam current (till 0.025 nA at 2 kV) to avoid ion beam damage. Additionally, a low current cleaning process (5–2 kV, 81-28 pA) was performed to remove any potential contamination.

Photovoltaic device characterization

Current density (J)-voltage (V) measurements were performed in ambient conditions under simulated AM1.5 G light with an intensity of 100 mW cm^{-2} (Wavelabs-Sinus 70). Intensity was calibrated using a calibrated Si reference cell (KG-3 filter Centronics LCE-50). Cells were scanned using a Keithley 2450 source-metre backward and forward from 1.5 V to −0.1 V, with a 100 mVs^{-1} scan speed (no dwell time or preconditioning applied). A shadow mask with an aperture of 0.03 cm^2 (measured through optical microscopy) was employed during the measurement. Operational stability tests were carried out by maximum power point tracking (MPPT) under AM1.5 G illumination (100 mW cm^{-2}) in N_2 atmosphere at room temperature. External quantum efficiency (EQE) measurements were performed with a Cicci Research s.r.l ARKEO steady-state tests module. Wavelength scan range was set between 300 and 900 nm with a scan step of 10 nm.

Average visible transmittance and light utilization efficiency computation

AVT has been calculated using Eq. 1 through the widely reported approach[57]:

$$AVT = \frac{\int_{380nm}^{800nm} T(\lambda)P(\lambda)S(\lambda)d\lambda}{\int_{380nm}^{800nm} P(\lambda)S(\lambda)d\lambda} \quad (1)$$

where λ is the wavelength, T is the device light transmission, P is the photopic response function, and S is the AM1.5 G solar irradiation.

LUE has been calculated as the product of AVT value and device power conversion efficiency (PCE), as presented in Eq. 2:

$$LUE = AVT \times PCE \quad (2)$$

Reporting summary

Further information on research design is available in the Nature Portfolio Reporting Summary linked to this article.

Data availability

The data generated in this study are available upon request from the corresponding author.

References

1. Grancini, G. & Nazeeruddin, M. K. Dimensional tailoring of hybrid perovskites for photovoltaics. *Nat. Rev. Mater.* **4**, 4–22 (2019).
2. Hou, J. et al. Synthesis of 2D perovskite crystals via progressive transformation of quantum well thickness. *Nat. Synth.* **3**, 265–275 (2024).
3. Romano, V. et al. Two-step thermal annealing: an effective route for 15% efficient quasi-2D perovskite solar cells. *ChemPlusChem* **86**, 1044–1048 (2021).
4. Wang, K., Wu, C., Yang, D., Jiang, Y. & Priya, S. Quasi-two-dimensional halide perovskite single crystal photodetector. *ACS Nano* **12**, 4919–4929 (2018).
5. Tsai, H. et al. High-efficiency two-dimensional ruddlesden-popper perovskite solar cells. *Nature* **536**, 312–317 (2016).
6. Ke, W. et al. Compositional and solvent engineering in Dion–Jacobson 2D perovskites boosts solar cell efficiency and stability. *Adv. Energy Mater.* **9**, 1803384 (2019).
7. Yue, T. et al. A binary solution strategy enables high-efficiency Quasi-2D perovskite solar cells with excellent thermal stability. *ACS Nano* **15**, 14632–14643 (2023).
8. Li, X. et al. Water-assisted crystal growth in quasi-2D perovskites with enhanced charge transport and photovoltaic performance. *Adv. Energy Mater.* **10**, 2001832 (2020).
9. Yang, R. et al. Oriented quasi-2D perovskites for high performance optoelectronic devices. *Adv. Mater.* **30**, 1804771 (2018).
10. Shi, J. et al. Fluorinated low-dimensional Ruddlesden–Popper perovskite solar cells with over 17% power conversion efficiency and improved stability. *Adv. Mater.* **31**, 1901673 (2019).
11. Zhang, F. et al. Enhanced charge transport in 2D perovskites via fluorination of organic cation. *J. Am. Chem. Soc.* **141**, 5972–5979 (2019).
12. Ren, H. et al. Efficient and stable Ruddlesden–Popper perovskite solar cell with tailored interlayer molecular interaction. *Nat. Photonics* **14**, 154–163 (2020).
13. Wu, G. et al. Molecular engineering for two-dimensional perovskites with photovoltaic efficiency exceeding 18%. *Matter* **4**, 582–599 (2021).
14. Dong, J. et al. Mechanism of crystal formation in Ruddlesden–Popper Sn-based perovskites. *Adv. Funct. Mater.* **30**, 2001294 (2020).
15. Quintero-Bermudez, R. et al. Compositional and orientational control in metal halide perovskites of reduced dimensionality. *Nat. Mater.* **17**, 900–907 (2018).
16. Cao, D. H., Stoumpos, C. C., Farha, O. K., Hupp, J. T. & Kanatzidis, M. G. 2D homologous perovskites as light-absorbing materials for solar cell applications. *J. Am. Chem. Soc.* **137**, 7843–7850 (2015).
17. Lai, H. et al. Two-dimensional Ruddlesden-Popper perovskite with nanorod-like morphology for solar cells with efficiency exceeding 15%. *J. Am. Chem. Soc.* **140**, 11639–11646 (2018).
18. Muhammad, B. T., Kar, S., Stephen, M. & Leong, W. L. Halide perovskite-based indoor photovoltaics: recent development and challenges. *Mater. Today Energy* **23**, 100907 (2022).
19. Bing, J. et al. Perovskite solar cells for building integrated photovoltaics—glazing applications. *Joule* **6**, 1446–1474 (2022).
20. Xu, F., Zhang, M., Li, Z., Yang, X. & Zhu, R. Challenges and perspectives toward future wide-bandgap mixed-halide perovskite photovoltaics. *Adv. Energy Mater.* **13**, 2203911 (2023).
21. Zhou, Y., Poli, I., Meggiolaro, D., De Angelis, F. & Petrozza, A. Defect activity in metal halide perovskites with wide and narrow bandgap. *Nat. Rev. Mater.* **6**, 986–1002 (2021).
22. Brennan, M. C., Ruth, A., Kamat, P. V. & Kuno, M. Photoinduced anion segregation in mixed halide perovskites. *Trends Chem.* **2**, 282–301 (2020).
23. Sidhik, S. et al. Memory seeds enable high structural phase purity in 2D perovskite films for high-efficiency devices. *Adv. Mater.* **33**, 2007176 (2021).
24. Chen, J. et al. Interfacial engineering enables high efficiency with a high open-circuit voltage above 1.23 v in 2D perovskite solar cells. *J. Mater. Chem. A Mater.* **6**, 18010–18017 (2018).
25. Zhu, X. H., Mercier, N., Riou, A., Blanchard, P. & Frère, P. (C4H3SCH2NH3)2(CH3NH3)Pb2I7: non-centrosymmetrical crystal structure of a bilayer hybrid perovskite. *Chem. Commun.* **2**, 2160–2161 (2002).
26. Dyksik, M. et al. Broad tunability of carrier effective masses in two-dimensional halide perovskites. *ACS Energy Lett.* **5**, 3609–3616 (2020).
27. Cho, C. et al. Efficient vertical charge transport in polycrystalline halide perovskites revealed by four-dimensional tracking of charge carriers. *Nat. Mater.* **21**, 1388–1395 (2022).
28. Magdaleno, A. J. et al. Efficient interlayer exciton transport in two-dimensional metal-halide perovskites. *Mater. Horiz.* **8**, 639–644 (2021).
29. Kim, M. et al. Methylammonium chloride induces intermediate phase stabilization for efficient perovskite solar cells. *Joule* **3**, 2179–2192 (2019).
30. Hu, J. et al. Iodine modulates the MACl-assisted growth of FAPbI3 for high efficiency perovskite solar cells. *Adv. Energy Mater.* **14**, 2400500 (2024).
31. Bi, L. et al. Deciphering the roles of MA-based volatile additives for α-FAPbI3 to enable efficient inverted perovskite solar cells. *J. Am. Chem. Soc.* **145**, 5920–5929 (2023).
32. Livakas, N. et al. CsPbCl3 → CsPbI3 exchange in perovskite nanocrystals proceeds through a jump-the-gap reaction mechanism. *J. Am. Chem. Soc.* **145**, 20442–20450 (2023).
33. Zhou, Y., Sternlicht, H. & Padture, N. P. Transmission electron microscopy of halide perovskite materials and devices. *Joule* **3**, 641–661 (2019).
34. Zhang, X. et al. Orientation regulation of phenylethylammonium cation based 2D perovskite solar cell with efficiency higher than 11. *Adv. Energy Mater.* **8**, 1702498 (2018).
35. Xiao, K. et al. Solution-processed monolithic all-perovskite triple-junction solar cells with efficiency exceeding 20%. *ACS Energy Lett.* **5**, 2819–2826 (2020).
36. Wang, Z. et al. Suppressed phase segregation for triple-junction perovskite solar cells. *Nature* **618**, 74–79 (2023).
37. Yang, Y. et al. Expanded phase distribution in low average layer-number 2D perovskite films: toward efficient semitransparent solar cells. *Adv. Funct. Mater.* **31**, 2104868 (2021).
38. Barichello, J. et al. Semi-transparent blade-coated FAPbBr3 perovskite solar cells: a scalable low-temperature manufacturing process under ambient condition. *Sol. RRL* **7**, 2200739 (2023).
39. Jiang, Z. GIXSGUI: A MATLAB toolbox for grazing-incidence X-ray scattering data visualization and reduction, and indexing of buried three-dimensional periodic nanostructured films. *J. Appl. Crystallogr.* **48**, 917–926 (2015).
40. Pica, G., Bajoni, D. & Grancini, G. A step beyond in steady-state and time-resolved electro-optical spectroscopy: Demonstration of a

customized simple, compact, low-cost, fiber-based interferometer system. *Struct. Dyn.* **9**, 011101 (2022).
41. Kresse, G. & Furthmuller, J. Efficiency of ab-initio total energy calculations for metals and semiconductors using a plane-wave basis set. *Comput. Mater. Sci.* **6**, 15–50 (1996).
42. Kresse, G. & Hafner, J. Ab. initio molecular dynamics for liquid metals. *Phys. Rev. B* **47**, 558–561 (1993).
43. Kresse, G. & Furthmü, J. Efficient iterative schemes for ab initio total-energy calculations using a plane-wave basis set. *Phys. Rev. B* **54**, 11169–11186 (1996).
44. Blochl, P. E. Projector augmented-wave method. *Phys. Rev. B* **50**, 17953–17979 (1994).
45. Perdew, J. P., Burke, K. & Ernzerhof, M. Generalized gradient approximation made simple. *Phys. Rev. Lett.* **77**, 3865–3868 (1996).
46. Grimme, S., Antony, J., Ehrlich, S. & Krieg, H. A consistent and accurate ab initio parametrization of density functional dispersion correction (DFT-D) for the 94 elements H-Pu. *J. Chem. Phys.* **132**, 154104 (2010).
47. Fonari, A. & Sutton, C. Effective Mass Calculator. Can be found under https://github.com/afonari/, nd (2012)
48. Grau-Crespo, R., Hamad, S., Catlow, C. R. A. & De Leeuw, N. H. Symmetry-adapted configurational modelling of fractional site occupancy in solids. *J. Phys. Condens. Matter* **19**, 256201 (2007).
49. Ångqvist, M. et al. ICET – A Python library for constructing and sampling alloy cluster expansions. *Adv. Theory Simul.* **2**, 1900015 (2019).
50. Sher, A., Van Schilfgaarde, M., Chen, A.-B. & Chen, W. Quasichemical approximation in binary alloys. *Phys. Rev. B* **36**, 4279–4295 (1987).
51. Kim, S., Eom, T., Ha, Y. S., Hong, K. H. & Kim, H. Thermodynamics of multicomponent perovskites: a guide to highly efficient and stable solar cell materials. *Chem. Mater.* **32**, 4265–4272 (2020).
52. Brivio, F., Caetano, C. & Walsh, A. Thermodynamic origin of photoinstability in the CH3NH3Pb(I1-xBrx)3 hybrid halide perovskite alloy. *J. Phys. Chem. Lett.* **7**, 1083–1087 (2016).
53. Jeon, J. et al. Polymorphic phase control mechanism of organic-inorganic hybrid perovskite engineered by dual-site alloying. *J. Phys. Chem. C.* **121**, 9508–9515 (2017).
54. Joyce, H. J., Boland, J. L., Davies, C. L., Baig, S. A. & Johnston, M. B. A review of the electrical properties of semiconductor nanowires: Insights gained from terahertz conductivity spectroscopy. *Semicond. Sci. Technol.* **31**, 103003 (2016).
55. Motti, S. G. et al. Exciton formation dynamics and band-like free charge-carrier transport in 2D metal halide perovskite semiconductors. *Adv. Funct. Mater.* **33**, 2300363 (2023).
56. Righetto, M. et al. Cation-disorder engineering promotes efficient charge-carrier transport in AgBiS2 nanocrystal films. *Adv. Mater.* **35**, 2305009 (2023).
57. Traverse, C. J., Pandey, R., Barr, M. C. & Lunt, R. R. Emergence of highly transparent photovoltaics for distributed applications. *Nat. Energy* **2**, 849–860 (2017).

Acknowledgements

The authors thank the University of Pavia through the programme "Dipartimenti di Eccellenza 2023–2027" and Fondazione Cariplo Economia Circolare 2021 Project (FLHYPER, no 20201067), funded under the "Circular Economy-2020" call. G.G. acknowledges the "HY-NANO" project that received funding from the European Research Council (ERC) Starting Grant 2018 under the European Union's Horizon 2020 research and innovation programme (Grant Agreement no. 802862) and the GOPV project (CSEAA_00011) which received funds from Bando Ricerca di Sistema - CSEA - TIPO A Piano triennale 2019 –2021 Decreto direttoriale 27 ottobre 2021 del Ministero della Transizione Ecologica; MASE-(ex MITE). The authors acknowledge the bilateral project CRG2022 - HERO2D/3D Perovskite Heterojunction Solar Cells: Pairing Performance with Stability. The authors acknowledge funding by the Engineering and Physical Sciences Research Council (EPSRC); U.K. M.S.I. and V. acknowledge the Engineering and Physical Sciences Research Council (EPSRC) Programme Grant (EP/X038777/1) for a postdoctoral fellowship and are grateful to the UK's HEC Materials Chemistry Consortium (EP/X035859/1) for the use of the ARCHER2 high-performance computing facilities. The authors acknowledge the use of the KAUST Core Labs facilities for some parts of device fabrication and TEM measurements. The authors are grateful for the technical support in TOF-SIMS measurement from Nano-X vacuum interconnected nanotech workstation (Nano-X) of Suzhou Institute of Nano-Tech and Nano-Bionics, Chinese Academy of Sciences (SINANO). L.M.H acknowledged financial support by the EPSRC. G.G.acknowledges Dr. Stefano Toso (IIT, Italy) for useful discussion.

Author contributions

Conceptualization: A.Z., V.L., V., S.D.W, M.S.I., G.G. Investigation: A.Z., V.L., V., F.T., B.V, K.A.E., J.D, A.S., F.F., G.P., M.P., S.M., C.D., B.K.Y., M. B., E.U., E.A. Resources: V.P. Data curation: S.M. Writing – original draft: A.Z., V.L., V., K.A.E., G.P. Writing – review & editing: M. B., E.U., E.A., C.Q.M., M.A.L., L.M.H., S.D.W., M.S.I., G.G. Visualization: V.L., V. Supervision: F.D., M.A.L., M.D.B., L.M.H., G.P., S.D.W., M.S.I., G.G.

Competing interests

A patent on the fabrication methodology of low-dimensional perovskites has been filed by the University of Pavia, with G.G. and A.Z. as inventors. The application number is 102022000025854. The patent is currently under examination. The other Authors declare no competing interests.

Additional information

Supplementary information The online version contains supplementary material available at https://doi.org/10.1038/s41467-024-53339-6.

Correspondence and requests for materials should be addressed to Giulia Grancini.

Peer review information *Nature Communications* thanks the anonymous reviewer(s) for their contribution to the peer review of this work. A peer review file is available.